Journal of Energy Chemistry 101 (2025) 16–22

Contents lists available at ScienceDirect

Journal of Energy Chemistry

journal homepage: www.elsevier.com/locate/jechem

http://www.journals.elsevier.com/
journal-of-energy-chemistry/

Unveiling solid-solid contact states in all-solid-state lithium batteries: An electrochemical impedance spectroscopy viewpoint

Jin-Liang Li [a], Liang Shen [a], Zi-Ning Cheng [a,d], Jun-Dong Zhang [a], Ling-Xuan Li [b], Yu-Tong Zhang [b], Yan-Bin Gao [a], Chunli Guo [d], Xiang Chen [a], Chen-Zi Zhao [a], Rui Zhang [b,c,*], Qiang Zhang [a,e,f,*]

[a] Tsinghua Center for Green Chemical Engineering Electrification, Beijing Key Laboratory of Green Chemical Reaction Engineering and Technology, Department of Chemical Engineering, Tsinghua University, Beijing 100084, China
[b] Advanced Research Institute of Multidisciplinary Science, School of Materials Science and Engineering, Beijing Institute of Technology, Beijing 100081, China
[c] Beijing Huairou Laboratory, Beijing 101400, China
[d] College of Materials Science and Engineering, Taiyuan University of Technology, Taiyuan 030024, Shanxi, China
[e] Institute for Carbon Neutrality, Tsinghua University, Beijing 100084, China
[f] Shanxi Research Institute for Clean Energy, Tsinghua University, Taiyuan 030032, Shanxi, China

ARTICLE INFO

Article history:
Received 10 September 2024
Revised 19 September 2024
Accepted 21 September 2024
Available online 30 September 2024

Keywords:
Electrochemical impedance spectroscopy
All-solid-state lithium batteries
Solid-solid contacts
Finite element method
Equivalent circuit model
Distribution of relaxation times

ABSTRACT

All-solid-state lithium batteries (ASSLBs) are strongly considered as the next-generation energy storage devices for their high energy density and intrinsic safety. The solid-solid contact between lithium metal and solid electrolyte plays a vital role in the performance of working ASSLBs, which is challenging to investigate quantitatively by experimental approach. This work proposed a quantitative model based on the finite element method for electrochemical impedance spectroscopy simulation of different solid-solid contact states in ASSLBs. With the assistance of an equivalent circuit model and distribution of relaxation times, it is discovered that as the number of voids and the sharpness of cracks increase, the contact resistance R_c grows and ultimately dominates the battery impedance. Through accurate fitting, inverse proportional relations between contact resistance R_c and (1 − porosity) as well as crack angle was disclosed. This contribution affords a fresh insight into clarifying solid-solid contact states in ASSLBs.

1. Introduction

With the growing global demand for clean energy and the advancement of transportation electrification, it is critical to promote the practical application of high-energy-density and intrinsically safe secondary batteries [1–5]. Compared to routine Li-ion batteries (LIBs), all-solid-state lithium batteries (ASSLBs) offer higher energy density and better safety performance for their use of non-flammable inorganic solid electrolytes (SEs) instead of organic liquid electrolytes, which makes them regarded as one of the most promising next-generation battery technologies [6–15].

The use of SEs in ASSLBs introduces abundant interfaces between solid particles [16], which induces various contact issues in a working battery [17,18]. During the charging and discharging cycles of ASSLBs, the interface between the lithium metal anode and SE often exhibits poor solid-solid contacts, including voids [19,20], dendrites [21–23], and cracks [24–26] during repeated charging/discharging. These poor contacts hinder the ion transport and electrode reactions, which renders huge impacts on the rate performance and the cycle stability of ASSLBs [27,28]. Consequently, it is vital to characterize and evaluate contact states of Li|SE interface in working ASSLBs.

As an electrochemical characterization method, electrochemical impedance spectroscopy (EIS) [29,30] is a potentially effective tool to evaluate contact states in working ASSLBs [31–34]. Through analyzing the EIS plot results, the processes of ion migration, interfacial contacts, charge transfer [35,36], and diffusion within working ASSLBs can be clarified and quantitatively probed. Furthermore, the equivalent circuit model (ECM) and distribution of relaxation times (DRT) [37,38] are two powerful models to

---

* Corresponding authors.
E-mail addresses: zr@hrl.ac.cn (R. Zhang), zhang-qiang@mails.tsinghua.edu.cn (Q. Zhang).

https://doi.org/10.1016/j.jechem.2024.09.035

quantitatively aid to EIS analysis. This affords detailed information on electrochemical properties in a working battery. Nevertheless, it is challenging to combine EIS characterization methods with actual solid-solid contact states, including the difficulty in predicting how the EIS plot evolves along with different solid-solid contact states, the inability to infer or diagnose the actual solid-solid contacts, and the actual working conditions [39]. These issues pose substantial challenges in quantitatively establishing the relationship between contact states and EIS.

With the rapid development of emerging computational or simulating methods [40], machine learning [41–43], density functional theory [44], molecular dynamics [45–48], phase field model [49–52], and finite element method (FEM) [53] are employed to investigate rechargeable batteries. Among them, FEM is a mesoscale numerical simulation tool advantageous in modeling the internal processes of batteries, which is strongly considered to simulate the electrochemical processes in ASSLBs accurately. By means of exploring the correspondence between the solid-solid contact states and EIS through FEM simulation quantitatively, the contact states of the internal interfaces in working ASSLBs can be effectively analyzed and diagnosed.

In this contribution, two-dimensional (2D) simulating model based on FEM to simulate EIS of different solid-solid contact states such as voids and cracks in ASSLBs was proposed. Through constructing the geometry morphologies of different interfacial contact states such as voids, dendrites, and cracks in the model and performing FEM simulation of EIS, Nyquist plots of different contact states can be acquired. With the assistance of the quantitative analysis of ECM and DRT, it is discovered that the more voids at the Li|SE interface, or the sharper the cracks formed by lithium dendrites, the higher the contact resistance (R_c) of ASSLBs will be. In addition, through analyses and fitting of simulation results, the inverse proportionality relation of the R_c with the variation of void porosity and crack angle is acquired, which affords a correlation between different contact states of the Li|SE interface in ASSLBs and EIS plots from the theoretical perspective (Fig. 1). Accordingly, it is expected to afford a basis for the preliminary judgment of the interfacial contact states within ASSLBs based on the shapes of the EIS plots and the magnitude of the R_c. This work affords quantitative rules for interpreting specific solid-solid contact states through experimental EIS results, offering a new perspective for revealing interfacial issues in ASSLBs.

2. Methodology

2.1. FEM simulation of EIS

The simulation of EIS for ASSLBs was performed using the lithium-ion battery module in COMSOL Multiphysics 5.5 platform by FEM. A 2D simulating model consisting of the lithium metal as anode, sulfide electrolyte Li_6SP_5Cl [54] as SE, and high-nickel layered oxide $LiNi_{0.8}Co_{0.1}Mn_{0.1}O_2$ (NCM811) as cathode was constructed (Fig. 2a). The properties of these energy materials in the model were taken from the COMSOL material library. The model includes the electron-conducting processes in electrodes, the ion transfer at the electrode/electrolyte interface, the mass transfer in the bulk, and the electrochemistry processes in electrodes. The detailed equations are elaborated as follows.

2.1.1. Domain equations

The battery domain obeys the Ohm's law.

$$\boldsymbol{j} = \sigma \nabla \varphi \tag{1}$$

where $\boldsymbol{j}$, σ, and φ represent the current density, ionic conductivity, and electric potential, respectively.

The diffusion of Li-ion can be depicted by Fick's 2nd law.

$$\frac{\partial c_{\mathrm{Li}^+}}{\partial t} = \nabla \cdot \left(D_{\mathrm{Li}^+} \nabla c_{\mathrm{Li}^+}\right) \tag{2}$$

where c_{Li^+} is the concentration of Li-ion and D_{Li^+} is the diffusion coefficient of Li-ion [55].

2.1.2. Electrode equations

The local current density j_{local} in the electrode is given by Butler-Volmer kinetic equation.

$$j_{\mathrm{local}} = j_0\left(\mathrm{e}^{\frac{(1-\alpha)F\eta}{RT}} - \mathrm{e}^{\frac{-\alpha F\eta}{RT}}\right) \tag{3}$$

where j_0 is the exchange current density, α is the transfer coefficient, F is the Faraday constant, R is the gas constant, T is the temperature, and η is the overpotential.

According to Faraday's law, the flux of Li-ion is proportional to the total electrode reaction current density, which gives

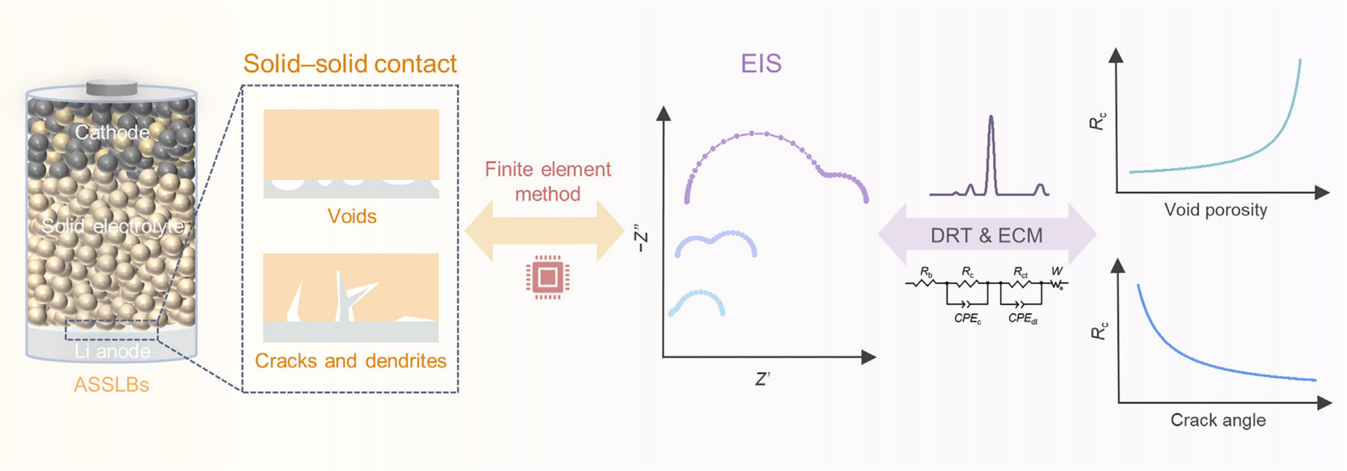

Fig. 1. Scheme of the correlation between solid-solid contact states and EIS simulation in ASSLBs. The Li|SE interface generates different contact states, such as voids, cracks, and dendrites, which are reflected in the EIS. Through the finite element method simulation of EIS and with the aid of ECM and DRT analysis, the relationships between the contact resistance R_c and void porosity as well as crack angle are clarified.

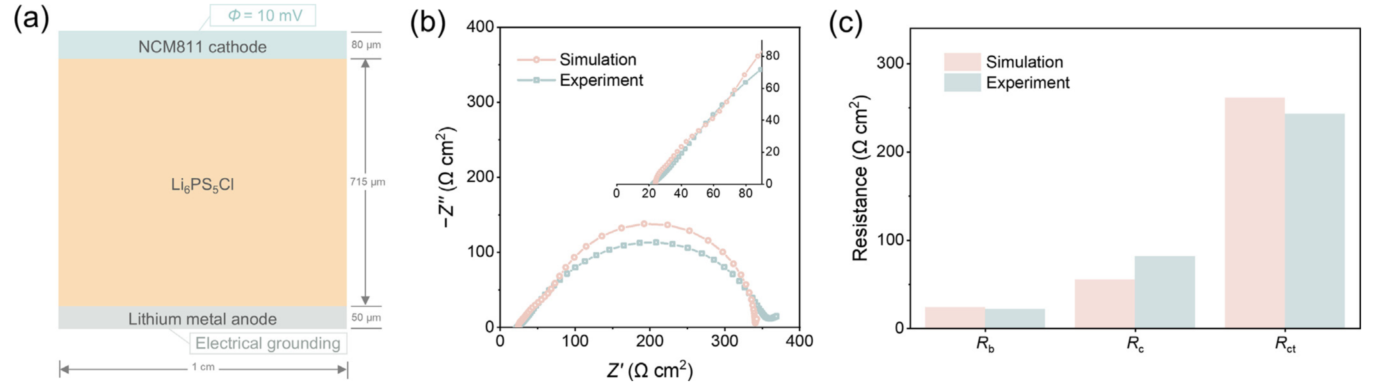

Fig. 2. The finite element method model of electrochemical impedance spectroscopy for all-solid-state lithium batteries. (a) The scheme of the constituent and boundary state of the model; (b) the Nyquist plot of simulated and experimental results; (c) ECM fitting of the bulk resistance, contact resistance, and charge transfer resistance for simulated and experimental EIS.

$$-\boldsymbol{n}\cdot\boldsymbol{N}_{\mathrm{Li}^+} = \frac{j_{\mathrm{v,total}}}{F} \tag{4}$$

where $\boldsymbol{N}_{\mathrm{Li}^+} = -D_{\mathrm{Li}^+}\nabla c_{\mathrm{Li}^+}$ is the flux of Li-ion.

The total current density

$$j_{\mathrm{v,total}} = a_{\mathrm{s}} j_{\mathrm{total}} \tag{5}$$

where $a_{\mathrm{s}} = \frac{3\varepsilon_1}{r_{\mathrm{p}}}$ is the active specific surface area of electrode material, ε_1 is the electrode volume fraction, and r_{p} is the particle size of electrode material.

The total interface current density

$$j_{\mathrm{total}} = \sum j_{\mathrm{local}} + j_{\mathrm{sl}} \tag{6}$$

where j_{local} is the local current density, $j_{\mathrm{sl}} = i\omega(\varphi - \Delta\varphi_{\mathrm{i}})C_{\mathrm{sl}}$ represents the contribution of the space-charge layer in ASSLBs, i is the imaginary unit, $\omega = 2\pi f$ is the angular frequency, $\Delta\varphi_{\mathrm{i}} = R_{\mathrm{i}} j_{\mathrm{total}}$ is the interface potential, and C_{sl} is the space-charge layer capacitance.

Based on Bruggeman empirical law and generalized Archie's empirical law [56–58], the calibration of conductivity in porous cathode can be written as

$$\sigma = \sigma_0 \varepsilon_2{}^{\gamma} \tag{7}$$

where σ represents the effective conductivity, σ_0 represents the intrinsic conductivity, ε_2 represents the volume fraction of electrolyte in electrode, and γ represents the Bruggeman coefficient of electrode respectively.

2.1.3. Boundary conditions

The anode current collector (lower boundary) is set to be electrical grounding, and the current density is specified at the cathode current collector (upper boundary) and a potential perturbation of Φ = 10 mV is applied. The left and right boundaries of the model are subject to insulated conditions.

2.1.4. Alternating current (AC) impedance study

All variables in AC steady state impedance study are displaced from time-dependent to frequency-dependent as shown in the following expression

$$n = n_0 + Re\left(\tilde{n}\cdot e^{2\pi f\,\cdot\, it}\right) \tag{8}$$

where n is the variable, and subscript 0 signifies the initial value, around which the perturbation takes place, and the wavy line indicates complex perturbations. i is the imaginary unit, f the frequency, and t the time.

The battery impedance $\tilde{Z}$ (Ω cm^2) at the boundary of the cathode current collector is calculated according to

$$\tilde{\varphi} = E_{\mathrm{eq}} + \Phi e^{-i\omega t} \tag{9}$$

$$\tilde{Z} = \frac{\tilde{\varphi}}{\boldsymbol{n}\cdot\tilde{\boldsymbol{j}}} \tag{10}$$

where $\tilde{\varphi}$ is the electric potential, E_{eq} is the equilibrium potential, $\Phi = 10\,\mathrm{mV}$ is the amplitude of potential perturbation, $\boldsymbol{n}$ is the normal vector to the boundary, and $\tilde{\boldsymbol{j}}$ is the current density in current collector.

The impedance is simulated in a frequency range from 0.1 Hz to 1 MHz. The detailed parameters for EIS simulation can be found in Table S1.

2.1.5. Void construction

Semi-ellipses of 25 μm in the long half-axis and 5 μm in the short half-axis are constructed as voids in the lithium metal anode and all the semi-ellipses are equidistantly distributed at the Li|SE interface. The porosity is defined as the ratio of the sum of the long axes of all half-ellipses to the total length of the interface (1 cm). The number of half-ellipses is given by the porosity as Number = porosity × (1 cm)/(50 μm).

2.1.6. Cracks construction

Isosceles triangles with a height of 10 μm are constructed as cracks on the SE of the Li|SE interface, and the triangle base is calculated from the height and apex angles. The triangles are equidistantly distributed at the interface, and the sum of the lengths of the base of all triangles accounts for 60% of the total length of the interface (1 cm). The sum of the areas of all the triangles is the same for different crack angles to simulate SE cracking caused by lithium dendrites of the same capacity.

2.2. Equivalent circuit model fitting

The equivalent circuit model for Li|Li$_6$PS$_5$Cl|NCM811 ASSLBs consists of four parts connected in series: the bulk resistor R_{b}, the contact resistor R_{c} parallel with constant phase element CPE$_{\mathrm{c}}$, the charge transfer resistor R_{ct} parallel with constant phase element CPE$_{\mathrm{dl}}$, and the Warburg element W corresponding to the diffusion process. The equivalent circuit fitting was performed using ZView software, starting with segmental fitting followed by global fitting.

2.3. Distribution of relaxation times

The DRT was realized using the MATLAB-GUI toolbox explored by Ciucci et al. [59]. The parameters used are listed in Table S2.

2.4. Experimental EIS measurements of ASSLBs

ASSLBs were assembled in an argon-filled glovebox (H_2O, $O_2 < 0.01$ ppm). NCM811 cathode (Saibo Co., Ltd) was mixed with Li_6PS_5Cl sulfide SE (Ganfeng Lithium Group Co., Ltd.) and conductive carbon at a mass ratio of 69:30:1. The mixtures were then hand-ground for 30 min in an agate mortar as the final cathode composite powders. Approximately 100 mg of Li_6PS_5Cl SE powder was first placed into the poly(ether-ether-ketone) cylinder with a 10 mm diameter and pressed at 400 MPa for 1 min, and then 7 mg composite cathode powder was spread on one side of Li_6PS_5Cl and pressed at 500 MPa for 1 min. Then, a Li foil (50 μm thickness, 10 mm diameter, China Energy Lithium Co., Ltd.) was attached to the other side of Li_6PS_5Cl. Ultimately, the ASSLB was placed into a custom-made stainless-steel casing. Galvanostatic cycling of the ASSLBs was conducted within the voltage range of 2.8–4.3 V vs. Li/Li^+ using a LAND-CT2001A (Wuhan, China). The rate for the first cycle was 0.05 C and that for the following cycles was 0.3 C. EIS measurement was performed on the Solartron EnergyLab XM with an amplitude of 10 mV and a frequency range from 0.1 Hz to 1 MHz after discharge of the 10th cycle.

3. Results and discussion

3.1. Model validation

The full-cell EIS of the typical ASSLB $Li|Li_6SP_5Cl|NCM811$ was simulated and compared with the experimentally measured EIS. The Nyquist plots and Bode plots at a frequency range from 0.1 Hz to 1 MHz are shown in Fig. 2(b) and Fig. S1. Both the Nyquist plots of simulation and experiment comprise three parts: a small semicircle at high-frequency region that corresponds to the interfacial contact, a large semicircle at medium and low-frequency region that corresponds to the charge transfer process, and a low-frequency region line that corresponds to the diffusion process. The simulated and experimental Nyquist plots are in good agreement, especially at the high-frequency region. Furthermore, the ECM fitting was conducted to both simulated and the experimental EIS (Fig. S2). The equivalent circuit for $Li|Li_6PS_5Cl|$NCM811 ASSLBs consists of four parts connected in series: the bulk resistor R_b, the contact resistor R_c parallel with constant phase element CPE_c, the charge transfer resistor R_{ct} parallel with constant phase element CPE_{dl}, and the Warburg element W [60–62]. The resistances of bulk, contact, and charge transfer for simulation and experiment are contrasted in Fig. 2(c). The R_b values are both in the range of 20–25 Ω cm^2, R_c in the range of 55–85 Ω cm^2, and R_{ct} in the range of 240–270 Ω cm^2 for simulation and experiment. The three resistance values of simulation and experiment exhibit good match, which confirms that the model can accurately reflect the impedance of $Li|Li_6SP_5Cl|NCM811$ and can be applied to explore the relationship between solid-solid contact states and EIS.

3.2. EIS evolution with the formation of voids

During the cycling of ASSLBs, lithium stripping [63] inevitably induces void formation at Li|SE interfaces [64], which induces poor contacts and ultimately a quick loss of battery capacity. Hence, it is essential to assess the state of the voids in working ASSLBs quantitatively, which is difficult to achieve by experimental measurements. To construct the correspondence between the void state and the EIS, the EIS of different void porosities was simulated by the model. The porosity of the Li|SE interface in 2D model is defined as the ratio of the sum of long axes lengths of all void half-ellipses at the interfaces to the total length of the interfaces.

The Nyquist plots of four typical scenarios of full contact (porosity = 0%), a few voids (porosity = 20%), numerous voids (porosity = 50%), and point contact (porosity = 100%) are shown in Fig. 3(a–d). When there is no void at the Li|SE interfaces, the Nyquist plot consists of a small semicircle representing the contact and a large semicircle representing the charge transfer. Once a few voids appear at the interfaces, the shape of the Nyquist plot changes with the semicircle representing the contact increasing in size while the semicircle representing the charge transfer remaining approximately the same in size, and the total impedance increases by around 100 Ω cm^2. As numerous voids are generated, the semicircle representing the contact increases significantly and exceeds the semicircle representing the charge transfer. The interfacial contact dominates the impedance, and the total impedance of the battery exceeds 1000 Ω cm^2. In the worst case, when the number of voids is so large that there is only point contact between Li and SE, the total impedance exceeds 1×10^6 Ω cm^2, and the entire Nyquist plot consists of a huge contact semicircle.

In order to further investigate the variation of EIS with porosity, EIS with the porosities of 0–100% was calculated (Fig. S3a). With the increase of porosity, the Nyquist plots exhibit a similar change pattern to that of Fig. 3(a–d), indicating that the diameter of the semicircle representing the contact gradually increases. Furthermore, the DRT analysis of porosity between 0% and 100% was performed (Fig. 3e and Fig. S4). The peaks of DRT at different relaxation times reflect the corresponding electrochemical processes, and the intensity and area of the peaks are positively correlated with the corresponding resistance magnitude [65]. The DRT plots of simulating EIS present four peaks: the peak around the relaxation time $\tau = 1 \times 10^{-5}$ s represents the bulk resistance R_b, the peak at $\tau = 1 \times 10^{-4}$–1×10^{-3} s represents the contact resistance R_c, the peak at $\tau = 1 \times 10^{-3}$–5×10^{-2} s represents the charge transfer resistance R_{ct}, and the peak around $\tau = 10$ s represents the diffusion resistance $R_{diffusion}$ [66,67]. As the porosity increases, the peaks of R_b and $R_{diffusion}$ show no significant change but the peak of R_c increases remarkably especially when the porosity is >60%. Besides, the peak of R_{ct} shifts to larger relaxation times, which indicates that the charge transfer process becomes more sluggish with the increase of porosity [68]. The changes of R_c and R_{ct} peaks can be attributed to the worse mass transfer and electrochemical reactions at the Li|SE interface caused by voids.

Additionally, ECM fittings were conducted with a porosity of 0–100% (Fig. S3b). The bulk resistance R_b increases with the porosity and undergoes a more pronounced change as porosity reaches the extreme case 100%, while the charge transfer resistance R_{ct} does not change significantly as porosity increases (Fig. S5). The contact resistance R_c increases considerably with porosity (Fig. 3f), which shares the same trend with DRT. As the porosity exceeds 80%, the profile increases more steeply. When porosity reaches 100%, the R_c tends to positive infinity. To improve the fitting accuracy, we add two points (porosity = 95% and 99%) at the increasing steepness of the curve. When the extreme case point of porosity = 100% is removed, R_c exhibits an inverse proportional function with (1 − porosity) and the R^2 of fitting reaches 0.998. The empirical fitting expression can be expressed as $R_c = 1.69 \times 10^3/(1 - \text{porosity}) - 1.64 \times 10^3$ (Ω cm^2). The empirical inverse proportional function indicates that the contact resistance R_c converges to around 50 Ω cm^2 when there are no voids (porosity = 0%). While the porosity is increased to the extreme case of 100%, R_c tends approximately to infinity, which can be attributed to the extremely poor mass transfer and electrode reactions at the interface led by

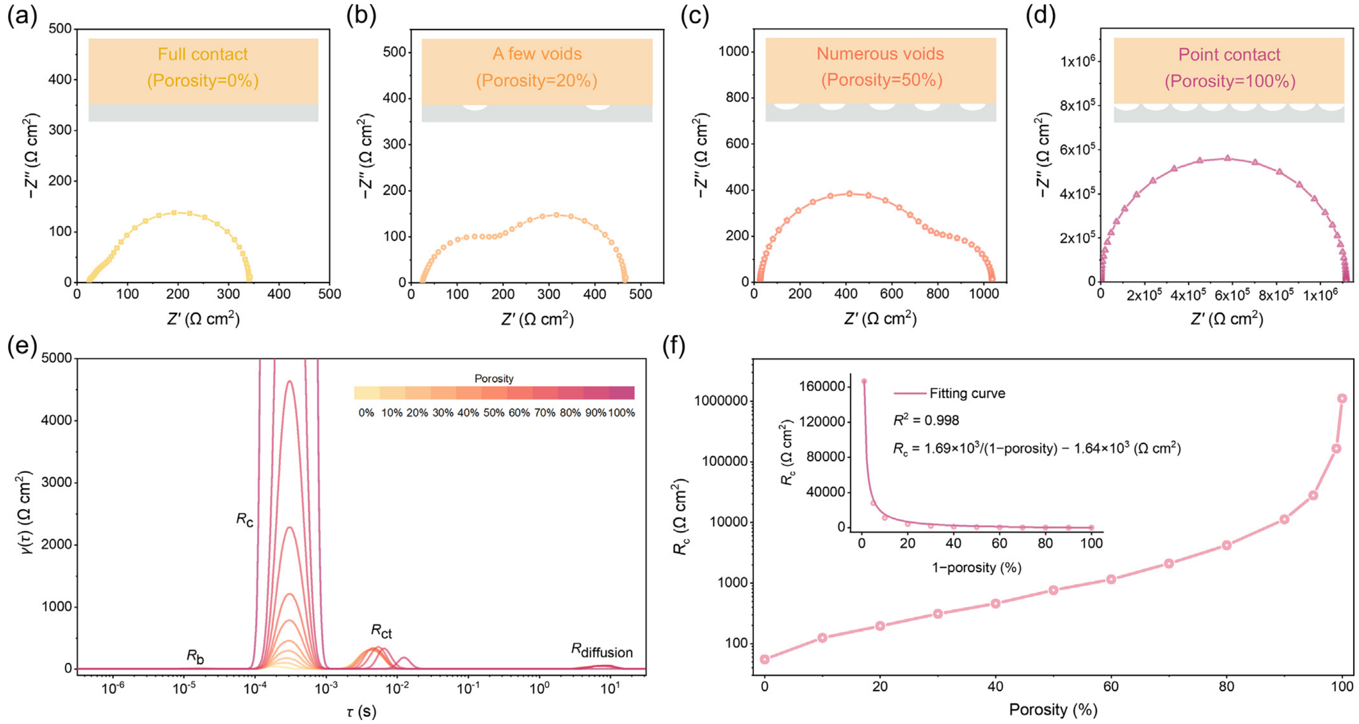

Fig. 3. The simulation of EIS and the related DRT and ECM analyses for different void porosities. (a–d) Schemes and Nyquist plots of four typical scenarios at Li|SE interface: full contact (porosity = 0%), a few voids (porosity = 20%), numerous voids (porosity = 50%), and point contact (porosity = 100%); (e) the DRT plots of different porosities ranging from 0% to 100%; (f) the relationship between contact resistance R_c and porosity. The inset represents the result of the inverse proportion function fitting.

poor contact. The inverse proportionality provides an empirical correlation between void porosity and contact resistance.

3.3. EIS evolution with the formation of Li dendrites

In addition to voids, lithium dendrites are generated during the cycling of ASSLBs [69,70]. The penetration of lithium dendrites into the SE always induces abundant cracks in SE [71,72], which can result in the increased resistance and degradation of capacity, and in severe cases, can cause short circuits of working batteries [73,74]. Therefore, it is expected to clarify the impact of cracks in ASSLBs. The EIS of cracks with different sharpness is therefore simulated to investigate the crack angle effect. In this model, triangular cracks with crack angles ranging from 160° to 20° are constructed, and it is ensured that the total area of the triangles at different crack angles is the same, that is, the capacity of the lithium dendrites is the same and the cracks accounted for 60% of the total interfacial contact area. The crack angle β is defined as the vertex angle of cracked triangles. Schematic diagram and Nyquist plots of crack angle ranging from 160° to 20° are shown in Fig. 4(a). As the crack angle decreases, the semicircle representing the contact gradually increases, and after the crack angle is less than 80°, the semicircle representing the contact exceeds the semicircle representing the charge transfer to occupy the main part of the impedance. The total impedance of the battery also increases threefold from 379 Ω cm^2 at 160° to 1553 Ω cm^2 at 20°, which indicates that the crack angle has a tremendous effect on the battery impedance.

Furthermore, DRT analysis was performed for crack angles ranging from 160° to 20° (Fig. 4b). With the reduction of crack angle, the peaks of R_b and $R_{diffusion}$ exhibit no obvious change and the peak of R_{ct} shifts slightly to larger relaxation times. In contrast, the peak of R_c increases remarkably, especially when the crack angle β is smaller than 90°. The effect caused by the crack angle on the EIS can be attributed to the fact that when the crack angle is smaller, the contact of Li|SE is sharper at the interface, and the resistance to mass transfer and electrochemical reaction at the interface is greater.

To further investigate the crack angle effect quantitatively, ECM fittings of crack angles ranging from 160° to 20° were conducted and shown in Fig. S6. The bulk resistance R_b remains around 30 Ω cm^2 and the charge transfer resistance R_{ct} remains around 245 Ω cm^2, both of which are unaffected by crack angle (Fig. S7). Unlike R_b and R_{ct}, the contact resistance R_c increases as the crack angle decreases, whose value grows from 107 Ω cm^2 at 160° to 1277 Ω cm^2 at 20° (Fig. 4c). Similar to the rule of void porosity, R_c presents an inverse proportional relation with crack angle (unit of radians), whose fitting expression is $R_c = 146\ \pi/\beta - 24.7$ (Ω cm^2). The R^2 of fitting reaches 0.998, demonstrating the accuracy of fitting. The crack angle effect illustrates that the sharp dendrites and cracks at Li|SE interface are more detrimental to ASSLBs. It is vital to enhance the flatness of SE and promote uniform lithium deposition in ASSLBs.

3.4. EIS evolution with solid-solid contact states

According to the simulated EIS of Li|Li_6PS_5Cl|NCM811 ASSLB, the EIS of different solid-solid contact states can be predicted. With the aid of ECM and DRT, correspondence between contact states at the Li|SE interface and EIS was established. For instance, two typical contact issues including voids and cracks in working ASSLBs were investigated. As the lithium void porosity increases, the semicircle representing the contact in EIS Nyquist plots is enlarged and the contact resistance R_c is increased. The bulk resistance R_b also increases with the porosity while the charge transfer resistance R_{ct} does not change significantly. However, the peak of R_{ct} in DRT shifts to higher relaxation times, which indicates that the charge transfer process becomes sluggish. The relationship between R_c and (1 − porosity) obeys the inverse proportional relation after fitting. It is hopeful to guide the preliminary judgment of void

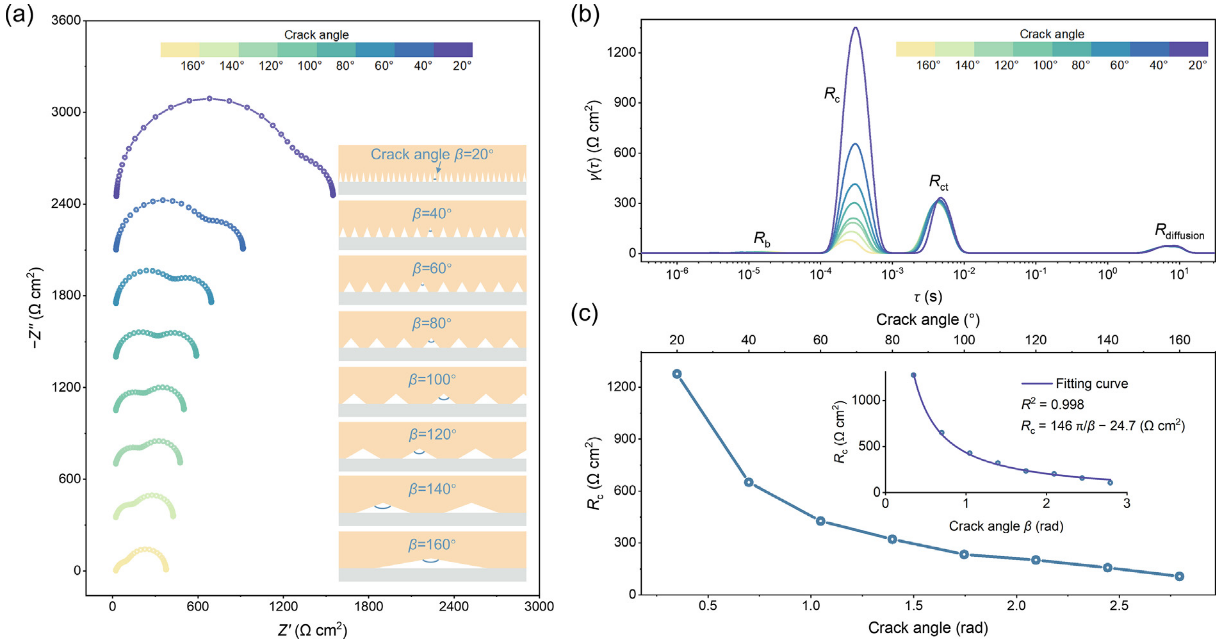

Fig. 4. The simulation of EIS and the related DRT and ECM analyses for different crack angles. (a) Schemes and Nyquist plots for different crack angles of 160°, 140°, 120°, 100°, 80°, 60°, 40°, and 20°; (b) the DRT plots of different crack angles from 160° to 20°; (c) the relationship between contact resistance R_c and crack angle. The inset represents the results of the inverse proportion function fitting, and the fitting unit of crack angle is radians.

conditions in working ASSLBs. The sharpness of crack induced by lithium dendrites affects the impedance of ASSLBs. The smaller the crack angle, the larger the contact resistance R_c, while the bulk resistance R_b and the charge transfer resistance R_{ct} have no remarkable changes. The R_c and crack angle β follow the inverse proportional relation as well. The crack angle effect gives an interpretation to eliminate sharp lithium dendrites and cracks in ASSLBs. Moreover, the model is expected to simulate more complex contact states inside the ASSLBs closer to its actual working conditions.

4. Conclusions

A 2D simulating model based on the finite element method for EIS simulation of different solid-solid contact states in ASSLBs has been proposed. We simulated the EIS of Li|Li_6PS_5Cl|NCM811 ASSLB, which corresponds well with the experimental results. Based on this model, EIS of different solid-solid contact states can be reproduced through simulation. With the aid of ECM and DRT, correspondence between contact states at the Li|SE interface and EIS was established. A relationship between R_c and (1 − porosity) obeys the inverse proportional relation after fitting which is expressed as $R_c = 1.69 \times 10^3/(1 - \text{porosity}) - 1.64 \times 10^3$ (Ω cm^2). The R_c and crack angle β follows the inverse proportional relation as well, whose fitting expression is $R_c = 146\ \pi/\beta - 24.7$ (Ω cm^2). This contribution affords a fresh approach to clarifying solid-solid contact states in ASSLBs. With these proposed quantitative rules, researchers can infer and diagnose the actual solid-solid contact states in ASSLBs from their EIS results. It is expected to inspire more attempts using simulation and computational tools to investigate interfacial problems of ASSLBs and give helpful guidance to design advanced ASSLBs with expected performance.

CRediT authorship contribution statement

Jin-Liang Li: Writing – review & editing, Writing – original draft, Visualization, Software, Investigation, Conceptualization. **Liang Shen:** Conceptualization, Formal analysis, Investigation. **Zi-Ning Cheng:** Methodology, Investigation. **Jun-Dong Zhang:** Formal analysis, Investigation. **Ling-Xuan Li:** Formal analysis, Investigation. **Yu-Tong Zhang:** Investigation. **Yan-Bin Gao:** Methodology, Visualization. **Chunli Guo:** Investigation, Resources. **Xiang Chen:** Writing – review & editing, Formal analysis, Investigation, Funding acquisition. **Chen-Zi Zhao:** Investigation, Funding acquisition, Resources. **Rui Zhang:** Writing – review & editing, Writing – original draft, Visualization, Validation, Supervision, Data curation, Conceptualization. **Qiang Zhang:** Writing – review & editing, Writing – original draft, Validation, Supervision, Resources, Conceptualization.

Declaration of competing interest

The authors declare that they have no known competing financial interests or personal relationships that could have appeared to influence the work reported in this paper.

Acknowledgments

This work was supported by the Beijing Natural Science Foundation (Z200011, L233004), the National Key Research and Development Program (2021YFB2500300), the National Natural Science Foundation of China (52394170, 52394171, 22109011, 22393900, and 22108151), the Tsinghua-Jiangyin Innovation Special Fund (TJISF) (2022JYTH0101), the S&T Program of Hebei (22344402D), and the Tsinghua University Initiative Scientific Research Program. The authors thank Yang Lu, Zong-Yao Shuang, Nan Yao, Yu-Chen Gao, Legeng Yu, Chao-Long Wang, Yu-Hang Yuan for helpful discussion.

Appendix A. Supplementary material

Supplementary material to this article can be found online at https://doi.org/10.1016/j.jechem.2024.09.035.

References

[1] D. Larcher, J.M. Tarascon, Nat. Chem. 7 (2015) 19–29.
[2] J.W. Choi, D. Aurbach, Nat. Rev. Mater. 1 (2016) 16013.
[3] L. Xu, Y. Lu, C.-Z. Zhao, H. Yuan, G.-L. Zhu, L.-P. Hou, Q. Zhang, J.-Q. Huang, Adv. Energy Mater. 11 (2021) 2002360.
[4] Y. Xu, Y. Du, H. Chen, J. Chen, T. Ding, D. Sun, D.H. Kim, Z. Lin, X. Zhou, Chem. Soc. Rev. 53 (2024) 7202–7298.
[5] J. Liao, X. Zhang, Q. Zhang, Q. Hu, Y. Li, Y. Du, J. Xu, L. Gu, X. Zhou, Nano Lett. 22 (2022) 4933–4940.
[6] J. Janek, W.G. Zeier, Nat. Energy 1 (2016) 16141.
[7] M.D. Tikekar, S. Choudhury, Z. Tu, L.A. Archer, Nat. Energy 1 (2016) 16114.
[8] R. Chen, Q. Li, X. Yu, L. Chen, H. Li, Chem. Rev. 120 (2020) 6820–6877.
[9] L. Xu, S. Tang, Y. Cheng, K. Wang, J. Liang, C. Liu, Y.-C. Cao, F. Wei, L. Mai, Joule 2 (2018) 1991–2015.
[10] P. Xu, Z.-Y. Shuang, C.-Z. Zhao, X. Li, L.-Z. Fan, A. Chen, H. Chen, E. Kuzmina, E. Karaseva, V. Kolosnitsyn, X. Zeng, P. Dong, Y. Zhang, M. Wang, Q. Zhang, Sci. China Chem. 67 (2024) 67–86.
[11] X.-B. Cheng, H. Liu, H. Yuan, H.-J. Peng, C. Tang, J.-Q. Huang, Q. Zhang, SusMat 1 (2021) 38–50.
[12] W.-Z. Huang, P. Xu, X.-Y. Huang, C.-Z. Zhao, X. Bie, H. Zhang, A. Chen, E. Kuzmina, E. Karaseva, V. Kolosnitsyn, X. Zhai, T. Jiang, L.-Z. Fan, D. Wang, Q. Zhang, MetalMat 1 (2024) e6.
[13] S.-J. Yang, F.-N. Jiang, J.-K. Hu, H. Yuan, X.-B. Cheng, S. Kaskel, Q. Zhang, J.-Q. Huang, Electron 1 (2023) e8.
[14] Z. Liu, W. Huang, Y. Xiao, J. Zhang, W. Kong, P. Wu, C. Zhao, A. Chen, Q. Zhang, Acta Phys. Chim. Sin. 40 (2024) 2305040.
[15] L. Kong, L. Wang, J. Zhu, J. Bian, W. Xia, R. Zhao, H. Lin, Y. Zhao, Chem. Commun. 57 (2021) 12587–12594.
[16] J. Hu, S. Yang, Y. Pei, X. Wang, Y. Liao, S. Li, A. Yue, J.-Q. Huang, H. Yuan, Particuology 86 (2024) 55–66.
[17] T. Famprikis, P. Canepa, J.A. Dawson, M.S. Islam, C. Masquelier, Nat. Mater. 18 (2019) 1278–1291.
[18] W. Mai, Q. Cao, M. Zheng, Y. Xiao, H. Hu, Y. Liu, Y. Liang, J. Energy Chem. 87 (2023) 491–500.
[19] P. Barai, T. Fuchs, E. Trevisanello, F.H. Richter, J. Janek, V. Srinivasan, Chem. Mater. 36 (2024) 2245–2258.
[20] V. Venturi, V. Viswanathan, ACS Energy Lett. 7 (2022) 1953–1959.
[21] J. Liu, H. Yuan, H. Liu, C.-Z. Zhao, Y. Lu, X.-B. Cheng, J.-Q. Huang, Q. Zhang, Adv. Energy Mater. 12 (2022) 2100748.
[22] V. Raj, V. Venturi, V.R. Kankanallu, B. Kuiri, V. Viswanathan, N.P.B. Aetukuri, Nat. Mater. 21 (2022) 1050–1056.
[23] L. Porz, T. Swamy, B.W. Sheldon, D. Rettenwander, T. Frömling, H.L. Thaman, S. Berendts, R. Uecker, W.C. Carter, Y.M. Chiang, Adv. Energy Mater. 7 (2017) 1701003.
[24] Y. Liu, X. Xu, X. Jiao, O.O. Kapitanova, Z. Song, S. Xiong, Adv. Mater. 35 (2023) 2301152.
[25] R.A. Ahmed, N. Ebechidi, I. Reisya, K. Orisekeh, A. Huda, A. Bello, O.K. Oyewole, W.O. Soboyejo, J. Power Sources 521 (2022) 230939.
[26] J. Adjah, K.I. Orisekeh, M. Vandadi, R.A. Ahmed, J. Asare, B. Agyei-Tuffour, D. Dodoo-Arhin, E. Nyankson, N. Rahbar, W.O. Soboyejo, J. Power Sources 613 (2024) 234873.
[27] C. Wang, J. Liang, Y. Zhao, M. Zheng, X. Li, X. Sun, Energy Environ. Sci. 14 (2021) 2577–2619.
[28] C. Yu, S. Ganapathy, E.R.H. van Eck, L. van Eijck, N. de Klerk, E.M. Kelder, M. Wagemaker, J. Energy Chem. 38 (2019) 1–7.
[29] S. Wang, J. Zhang, O. Gharbi, V. Vivier, M. Gao, M.E. Orazem, Nat. Rev. Methods Primers 1 (2021) 41.
[30] P. Vadhva, J. Hu, M.J. Johnson, R. Stocker, M. Braglia, D.J.L. Brett, A.J.E. Rettie, ChemElectroChem 8 (2021) 1930–1947.
[31] E.J. Cheng, Y. Kushida, T. Abe, K. Kanamura, ACS Appl. Mater. Interfaces 14 (2022) 40881–40889.
[32] X. Li, H. Guan, Z. Ma, M. Liang, D. Song, H. Zhang, X. Shi, C. Li, L. Jiao, L. Zhang, J. Energy Chem. 48 (2020) 195–202.
[33] L. Zhang, Y. Dai, C. Li, Y. Dang, R. Zheng, Z. Wang, Y. Wang, Y. Cui, H. Arandiyan, Z. Shao, H. Sun, Q. Zhuang, Y. Liu, Energy Stor. Mater. 69 (2024) 103378.
[34] Y. Yin, X. Qiu, Z. Dai, X. Guo, Solid State Ion 399 (2023) 116311.
[35] Y. Bai, Q.-A. Huang, K. Wu, J. Zhang, J. Energy Chem. 92 (2024) 759–798.
[36] J.-Y. Duan, J.-X. Chen, F.-F. Wang, J.-H. Zhang, X.-Z. Fan, L. Wang, Y. Song, W. Xia, Y. Zhao, L. Kong, J. Energy Chem. 87 (2023) 473–478.
[37] Y. Lu, C.-Z. Zhao, J.-Q. Huang, Q. Zhang, Joule 6 (2022) 1172–1198.
[38] A. Maradesa, B. Py, J. Huang, Y. Lu, P. Iurilli, A. Mrozinski, H.M. Law, Y. Wang, Z. Wang, J. Li, S. Xu, Q. Meyer, J. Liu, C. Brivio, A. Gavrilyuk, K. Kobayashi, A. Bertei, N.J. Williams, C. Zhao, M. Danzer, M. Zic, P. Wu, V. Yrjänä, S. Pereverzyev, Y. Chen, A. Weber, S.V. Kalinin, J.P. Schmidt, Y. Tsur, B.A. Boukamp, Q. Zhang, M. Gaberšček, R. O'Hayre, F. Ciucci, Joule 8 (2024) 1958–1981.
[39] X.-S. Zhang, J. Wan, Z.-Z. Shen, S.-Y. Lang, S. Xin, R. Wen, Y.-G. Guo, L.-J. Wan, Angew. Chem. Int. Ed. 63 (2024) e202409435.
[40] R. Zhang, X. Shen, Y.-T. Zhang, X.-L. Zhong, H.-T. Ju, T.-X. Huang, X. Chen, J.-D. Zhang, J.-Q. Huang, J. Energy Chem. 71 (2022) 29–35.
[41] C. Han, Y.-C. Gao, X. Chen, X. Liu, N. Yao, L. Yu, L. Kong, Q. Zhang, InfoMat 6 (2024) e12521.
[42] Y.-C. Gao, N. Yao, X. Chen, L. Yu, R. Zhang, Q. Zhang, J. Am. Chem. Soc. 145 (2023) 23764–23770.
[43] N. Yao, X. Chen, Z.-H. Fu, Q. Zhang, Chem. Rev. 122 (2022) 10970–11021.
[44] X. Chen, Y.-K. Bai, X. Shen, H.-J. Peng, Q. Zhang, J. Energy Chem. 51 (2020) 1–6.
[45] X. Chen, X. Shen, T.-Z. Hou, R. Zhang, H.-J. Peng, Q. Zhang, Chem 6 (2020) 2242–2256.
[46] L. Yu, X. Chen, N. Yao, Y.-C. Gao, Q. Zhang, J. Mater. Chem. A 11 (2023) 11078–11088.
[47] L. Yu, N. Yao, Y.-C. Gao, Z.-H. Fu, B. Jiang, R. Li, C. Tang, X. Chen, J. Energy Chem. 93 (2024) 299–305.
[48] N. Yao, L. Yu, Z.-H. Fu, X. Shen, T.-Z. Hou, X. Liu, Y.-C. Gao, R. Zhang, C.-Z. Zhao, X. Chen, Q. Zhang, Angew. Chem. Int. Ed. 62 (2023) e202305331.
[49] X. Shen, R. Zhang, P. Shi, X. Chen, Q. Zhang, Adv. Energy Mater. 11 (2021) 2003416.
[50] R. Zhang, X. Shen, X.-B. Cheng, Q. Zhang, Energy Stor. Mater. 23 (2019) 556–565.
[51] R. Zhang, X. Shen, H.-T. Ju, J.-D. Zhang, Y.-T. Zhang, J.-Q. Huang, J. Energy Chem. 73 (2022) 285–291.
[52] L. Chen, H.W. Zhang, L.Y. Liang, Z. Liu, Y. Qi, P. Lu, J. Chen, L.-Q. Chen, J. Power Sources 300 (2015) 376–385.
[53] X. Shen, R. Zhang, X. Chen, X.B. Cheng, X. Li, Q. Zhang, Adv. Energy Mater. 10 (2020) 1903645.
[54] H.-J. Deiseroth, S.-T. Kong, H. Eckert, J. Vannahme, C. Reiner, T. Zaiß, M. Schlosser, Angew. Chem. Int. Ed. 47 (2008) 755–758.
[55] Q.-A. Huang, Y. Bai, L. Wang, J. Wang, F. Zhang, L. Wang, X. Li, J. Zhang, J. Energy Chem. 67 (2022) 209–224.
[56] D.A.G. Bruggeman, Ann. Phys. 416 (1935) 636–664.
[57] G.E. Archie, Trans. AIME 146 (1942) 54–62.
[58] Z. Yan, L. Wang, H. Zhang, X. He, Adv. Energy Mater. 14 (2024) 2303206.
[59] T.H. Wan, M. Saccoccio, C. Chen, F. Ciucci, Electrochim. Acta 184 (2015) 483–499.
[60] Y.-W. Song, Y.-Q. Peng, M. Zhao, Y. Lu, J.-N. Liu, B.-Q. Li, Q. Zhang, Small Sci. 1 (2021) 2100042.
[61] S. Wenzel, S.J. Sedlmaier, C. Dietrich, W.G. Zeier, J. Janek, Solid State Ion 318 (2018) 102–112.
[62] J. Zhang, C. Zheng, L. Li, Y. Xia, H. Huang, Y. Gan, C. Liang, X. He, X. Tao, W. Zhang, Adv. Energy Mater. 10 (2020) 1903311.
[63] F.-N. Jiang, S.-J. Yang, H. Liu, X.-B. Cheng, L. Liu, R. Xiang, Q. Zhang, S. Kaskel, J.-Q. Huang, SusMat 1 (2021) 506–536.
[64] Y. Lu, C.-Z. Zhao, J.-K. Hu, S. Sun, H. Yuan, Z.-H. Fu, X. Chen, J.-Q. Huang, M. Ouyang, Q. Zhang, Sci. Adv. 8 (2022) eadd0510.
[65] S. Sun, C.-Z. Zhao, H. Yuan, Z.-H. Fu, X. Chen, Y. Lu, Y.-F. Li, J.-K. Hu, J. Dong, J.-Q. Huang, M. Ouyang, Q. Zhang, Sci. Adv. 8 (2022) eadd5189.
[66] C. Plank, T. Rüther, L. Jahn, M. Schamel, J.P. Schmidt, F. Ciucci, M.A. Danzer, J. Power Sources 594 (2024) 233845.
[67] C.-Y. Yu, J. Choi, J. Dunham, R. Ghahremani, K. Liu, P. Lindemann, Z. Garver, D. Barchiesi, R. Farahati, J.-H. Kim, J. Power Sources 597 (2024) 234116.
[68] J. Chen, E. Quattrocchi, F. Ciucci, Y. Chen, Chem 9 (2023) 2267–2281.
[69] Y.-L. Liao, J.-K. Hu, Z.-H. Fu, C.-Z. Zhao, Y. Lu, S. Li, S.-J. Yang, S. Sun, X.-L. Wang, J. Liu, J.-Q. Huang, H. Yuan, J. Energy Chem. 80 (2023) 458–465.
[70] Q. Gao, D. Wu, Z. Wang, P. Lu, X. Zhu, T. Ma, M. Yang, L. Chen, H. Li, F. Wu, Energy Stor. Mater. 63 (2023) 103007.
[71] Z. Ning, D.S. Jolly, G. Li, R. De Meyere, S.D. Pu, Y. Chen, J. Kasemchainan, J. Ihli, C. Gong, B. Liu, D.L.R. Melvin, A. Bonnin, O. Magdysyuk, P. Adamson, G.O. Hartley, C.W. Monroe, T.J. Marrow, P.G. Bruce, Nat. Mater. 20 (2021) 1121–1129.
[72] C. Yuan, W. Lu, J. Xu, Adv. Energy Mater. 11 (2021) 2101807.
[73] M. Otoyama, M. Suyama, C. Hotehama, H. Kowada, Y. Takeda, K. Ito, A. Sakuda, M. Tatsumisago, A. Hayashi, ACS Appl. Mater. Interfaces 13 (2021) 5000–5007.
[74] C. Wang, T. Deng, X. Fan, M. Zheng, R. Yu, Q. Lu, H. Duan, H. Huang, C. Wang, X. Sun, Joule 6 (2022) 1770–1781.